Correlation of Interface Structure with Magnetic Exchange in a Hard/Soft Magnetic Model Nanostructure

S. Sabet,[1,*] A. Moradabadi,[1] S. Gorji,[2,3] M.H. Fawey,[2,3] E. Hildebrandt,[1] I. Radulov,[1] D. Wang,[2,4] H. Zhang,[1] C. Kübel,[2,4] and L. Alff[1]

[1] *Institute of Materials Science, Technische Universität Darmstadt, 64287 Darmstadt, Germany*

[2] *Institute of Nanotechnology (INT), Karlsruhe Institute of Technology (KIT), 76344 Eggenstein-Leopoldshafen, Germany*

[3] *Joint Research Laboratory Nanomaterials (KIT and TUD), Technische Universität Darmstadt, 64287 Darmstadt, Germany*

[4] *Karlsruhe Nano Micro Facility, Karlsruhe Institute of Technology (KIT), 76344 Eggenstein-Leopoldshafen, Germany*

(Received 5 October 2018; revised manuscript received 10 March 2019; published 29 May 2019)

Synthesis of hard/soft magnetically exchange-coupled heterostructures is one promising way to design energy-efficient rare-earth-free artificial magnetic materials for application as permanent magnets and in spintronics. As a model system, we experimentally investigate MnGa/FeCo bilayers and simulate their physical behavior in a combined density functional theory and micromagnetic approach. Using high-quality $L1_0$-$Mn_{1.5}Ga$ thin films with bulklike magnetic properties, we show that optimal coherent exchange coupling is obtained below a critical soft magnetic layer thickness that depends on the interface structure and composition. In particular, for atomically smooth and matched epitaxial interfaces of $L1_0$-$Mn_{1.5}Ga$ to a Co-terminated and Co-rich FeCo layer, coherent exchange coupling is observed for FeCo thicknesses below 2 nm. In optimized bilayers, the magnetic coercivity of MnGa (approximately 6 kOe) can be fully conserved while the overall saturation magnetization is increased beyond 1000 emu/cm^3. Our model correlates interface structure and magnetic exchange coupling, providing guidelines to engineer high-performance exchange-coupled heterostructures for permanent magnets or spintronic devices.

DOI: 10.1103/PhysRevApplied.11.054078

I. INTRODUCTION

The key idea behind exchange spring magnets or hard/soft magnetically coupled nanostructures is to combine the large hysteresis of a hard magnetic material with high-saturation magnetization of a soft magnetic material in an artificial heterosystem [1]. Such composites or heterosystems possess a larger energy product, making them suitable for energy efficient and sustainable permanent magnets. For the soft magnetic material, iron cobalt alloys are a straightforward choice as they give the highest magnetization per volume. For the hard magnetic material, there are several candidates, among which the Mn-based intermetallics with large hysteresis but moderate magnetization are cost efficient and therefore favorable candidates.

Mn-based ferromagnetic phases such as MnGa, MnAl, and MnBi with their strong perpendicular anisotropy, high Curie temperature, and spin polarization are promising candidates for applications in spintronics and magnetic recording [2,3]. As perpendicular magnetic recording strives to reach higher density data storage in the range of 10 Tb/inch^2, thin films with large perpendicular magnetic anisotropy, K_u, of at least 10^7 erg/cm^3, as well as a moderate saturation magnetization, M_s, are required [4,5]. Therefore, synthesis of Mn-based ferromagnetic thin films has recently attracted much attention in research [6–22].

Despite all previous efforts, the magnetic properties are not yet close to the predicted values, leaving room for improvement of MnGa thin films [7,8,19,23–31]. To our best knowledge, the highest reported values of magnetic anisotropy and saturation magnetization for $L1_0$-MnGa (001) thin films are 15 Merg/cm^3 and 600 emu/cm^3, respectively, measured for sputtered thin films grown onto MgO(100) substrates (with a lattice misfit of 7.8%) covered by a Cr(100) buffer layer (with a lattice misfit of 4.6%) [7]. Not only improvements in growth and magnetic properties of Mn_xGa thin films is beneficial itself to spur applications, but synthesis of exchange-coupled magnets with the Mn_xGa as a hard magnetic phase is also advantageous in order to achieve larger energy products [1,32–37].

*sabet@oxide.tu-darmstadt.de

It has been previously shown that the Co contents in the FeCo soft magnetic layer are crucial for the sign of the magnetic coupling in a MnGa/FeCo system, where a transition from ferromagnetic to antiferromagnetic coupling has been observed [38]. For the MnBi/FeCo system, it was found that the interface roughness is an important parameter affecting exchange coupling [39,40]. Moreover, the effect of intermixing close to the exchange interface caused by the application of a substrate or annealing temperature has been previously studied in SmCo/Fe(Co) exchange system, which has resulted in an improvement of exchange coupling in this case [41,42].

In this study, we present improved magnetic properties in phase-pure $L1_0$-$Mn_{1.5}Ga$ epitaxial films. Moreover, we employ a combined experimental and theoretical approach to investigate the influence of different structural factors such as soft layer thickness, interface structure, and composition on the exchange properties in MnGa/FeCo bilayers. The result of our investigation offers a possibility to gain even higher magnetic properties through engineering of the exchange interface. These room-temperature magnetic properties make our $L1_0$-$Mn_{1.5}Ga$ thin films and exchange-coupled bilayers economical candidates not only for permanent magnet applications but also for high-density magnetic storage and spintronic devices.

II. EXPERIMENTAL PROCEDURE

MnGa thin films with thicknesses of approximately 40 nm are deposited onto Cr-buffered MgO(100) single crystal substrates in a dc magnetron sputtering system with a base pressure of approximately 4.0×10^{-6} Pa. The substrates are heated to 650 °C under vacuum for 30 min prior to deposition for surface cleaning. After cooling down to room temperature and heating again to 350 °C, a Cr buffer layer of 25-nm thickness is deposited from a 3-mm-thick Cr target (99.99%). The optimum growth parameters for the Cr buffer layer are 2.5-Pa Ar gas pressure at 20-W sputtering power and a substrate-to-source distance of 15 cm, leading to a growth rate of 0.017 nm/s. In the next step, the MnGa layer is deposited using an alloy target with a composition of $Mn_{60}Ga_{40}$ (at. %). The substrate temperature T_s is varied from 350 °C to 600 °C. The optimum growth parameters for deposition of MnGa layer with a minimum deposition rate of 0.04 nm/s are found to be 0.8-Pa Ar gas pressure at 20-W sputtering power with a target-to-substrate distance of 15 cm. The temperature is ramped up and down with a rate of 20 °C/min and 10 °C/min, respectively. At the final step, after cooling to 100 °C, the MnGa thin films are capped with a 5-nm-thick Cr layer to protect them against oxidation. The optimum growth parameters for the FeCo layer are as follows: 2.5-Pa Ar gas pressure at 80-W sputtering power with a target-to-substrate distance of 8 cm at a substrate temperature of 100 °C, which leads to a deposition rate of 0.008 nm/s. The FeCo layers with thicknesses between 2 and 8 nm are deposited from an alloy $Fe_{65}Co_{35}$ (at. %) target.

The phase composition and degree of crystallinity for the MnGa films are determined by X-ray diffraction with Cu $K\alpha$ radiation using a Rigaku SmartLab thin-film diffractometer. The film thickness is determined by a Bruker Dektak-XT stylus surface profiling system. The magnetic properties are measured by super quantum interference device (SQUID) magnetometer (MPMS, QuantumDesign). The angular dependence of the magnetic torque is measured using a torque magnetometer attached to a Physical Property Measurement System (PPMS) device (QuantumDesign). For cross-sectional high resolution-transmission electron microscopy (HR-TEM) investigations, TEM lamellae are prepared by a focused ion beam (FIB) using a FEI Strata 400S equipped with an OmniProbe 200 micromanipulator for *in situ* lift-out. TEM sample preparation is initially performed at 30 kV with an ion beam current of 16 nA, followed by cleaning with a 6.5-nA ion beam current. The final thinning step of the area of interest at the interface is performed at a low voltage starting from 8 to 2 kV with ion beam currents ranging from 56 to 3 pA. An aberration-corrected FEI Titan 80-300 operating at 300-kV acceleration voltage and equipped with a US1000 slow-scan CCD camera (Gatan Inc.), a high-angle annular dark-field (HAADF) detector (Fischione), and an super ultra-thin window (SUTW) energy-dispersive X-ray (EDX) detector (EDAX Inc.) is used to evaluate the interface structure and composition.

III. THEORETICAL PROCEDURE

A. Density functional theory

Ab initio-based calculations are performed in the framework of density functional theory (DFT) using the VASP code [43]. Exchange and correlation energies are approximated based on the method proposed by Perdew, Burke, and Ernzerhof (GGA-PBE) [44]. For the bulk structures, tetragonal MnGa ($P4/mmm$, $a = b = 2.711$ Å, and $c = 3.663$ Å) and alloy structures of cubic Fe_3Co_5 and Fe_5Co_3 ($Im\bar{3}m$, $a = b = c = 5.741$ Å) are considered. After the full geometry optimization for bulk MnGa and FeCo, two MnGa/FeCo interface models are constructed, MnGa(001)/Fe_3Co_5(001) and MnGa(001)/Fe_5Co_3(001), using a 2×2 supercell of MnGa(001) and a 1×1 unit cell of FeCo(001) with 88 atoms in total. We construct symmetric and nonstoichiometric slabs so that their corresponding interface formation energies are comparable. The thicknesses of the MnGa and FeCo layers in our models are approximately 1.5 and 1.8 nm, respectively. In addition, the atomic layers in 1/3 of the bottom of the MnGa layer are kept fixed during structural optimization. A 14-Å vacuum is considered between the periodic images to minimize any artificial interactions.

In order to compare the thermodynamic stability of different interfaces, the formation energy γ_{int} is calculated using the following equation:

$$\gamma_{\text{int}} = \frac{1}{2S}\left[E_{\text{int}} - n_1 E_{\text{bulk}}^{\text{MnGa}} - n_2 E_{\text{bulk}}^{\text{FeCo}} + \sum_i \mu_i\right], \quad (1)$$

where S, E_{int}, $E_{\text{bulk}}^{\text{MnGa}}$, and $E_{\text{bulk}}^{\text{FeCo}}$ are the area, the total energy of the relaxed interface, and the total energies per formula unit of bulk MnGa and FeCo, respectively. In addition, μ_i, n_1, and n_2 are the chemical potential and the number of bulk units of MnGa and FeCo in the models, respectively. The chemical potential corresponds to any missing atoms in our model and is obtained from total energies per atom in metallic bulks of Mn, Ga, Fe, and Co.

The lattice mismatch between MnGa(001) and FeCo(001) after cell optimization is approximately 4.2%. For the MnGa(001)/FeCo(001) interface, a $3 \times 3 \times 1$ k-points mesh is used. The energy cutoff for all the calculations is 500 eV. Convergence tests of the energy cutoff and k-point mesh with respect to the force of 0.03 eV Å^{-1} per atom are performed.

B. Micromagnetic simulation

Micromagnetic simulations are performed to investigate the effect of the soft layer thickness. We use the DFT results as input for the three-dimensional (3D) NIST object oriented micromagnetic framework (OOMMF) code [45]. In our model, the thickness of the hard MnGa layer is set as 40 nm. The thickness of the soft FeCo layer is changed in the range of 0.5–8 nm. The lateral size is chosen as 8×8 nm^2 and an in-plane periodic boundary condition is applied. The model is discretized by $0.4 \times 0.4 \times 0.1$-nm cuboid cells. Magnetic reversal curves are calculated by setting the initial magnetization along the positive z axis and changing the external magnetic field along z from 0.5 to -0.5 T.

The bulk parameters for exchange stiffness A, K_u, and M_s are set as the following values: $A^{\text{FeCo}} = 10$ pJ/m [46], $A^{\text{MnGa}} = 10$ pJ/m [47], $K^{\text{FeCo}} = 0$ MJ/m^3 [46], $K^{\text{MnGa}} = 2.1$ MJ/m^3 (using our experimental data), $M_s^{\text{FeCo}} = 2.47$ T, and $M_s^{\text{MnGa}} = 1.05$ T. The last two values of M_s are obtained from DFT calculations. Then the interface exchange coupling energy J^{int} is estimated by the expression $J^{\text{int}} = (E^{\text{AFM}} - E^{\text{FM}})/S$, in which E^{AFM} and E^{FM} are the interface total energies for antiferromagnetic (AFM) and ferromagnetic (FM) configurations, respectively, obtained from DFT calculations. The expression for calculating J^{int} was previously used in the literature [48,49].

In order to characterize the degree of exchange coupling between MnGa and FeCo layers through the interface, the exchange stiffness constant A^{int} is estimated according to the method presented in the OOMMF code [45]. According to this approach, the contribution of exchange energy density is numerically expressed as [45]

$$E_i = \sum_{j \epsilon N_i} A_{ij} \frac{\vec{m}_i \cdot (\vec{m}_i - \vec{m}_j)}{\Delta_{ij}^2}. \quad (2)$$

Here, E_i is the exchange energy density of cell i, A_{ij} is the exchange parameter between two cells, $\vec{m}_i$ and $\vec{m}_j$ are the magnetization unit vectors of the two i and j cells, and Δ_{ij}^2 is the discretization steps between two cells. Thus, the variation of micromagnetic exchange energy density can be approximated by $\delta E_i \cong 2A^{\text{int}}/\Delta z^2$, in which $\Delta z = 0.1$ nm is the distance between the two adjacent grid cells along the z direction.

The energy density difference (δE_i) from numerical approximation is assumed to be equal to that obtained from DFT calculations as follows:

$$\delta E_i \approx I^{\text{vol}} = J^{\text{int}}/\Delta d, \quad (3)$$

where I^{vol} is the volumetric energy density based on *ab initio*-based calculations. Δd is the average distance at the interface estimated from the relaxed interface structures. Finally, the interface exchange stiffness constant can be estimated using the following equation:

$$2A^{\text{int}}/\Delta z^2 = I^{\text{vol}} = J^{\text{int}}/\Delta d. \quad (4)$$

The resulting values of γ^{int}, J^{int}, and I^{int} are shown in Table I.

TABLE I. Values of interface formation energy γ^{int}, interface exchange coupling energy J^{int}, interface exchange constant A^{int}, and lattice mismatch calculated by DFT considering different compositions of Fe_xCo_{1-x} layer and different terminations at the MnGa/FeCo interface. All the interfaces are perpendicular to the [001] crystallographic direction.

Composition	Interface strain	Interface termination of soft layer	γ^{int} (eV/Å^2)	J^{int} (J/m^2)	A^{int} (pJ/m)
MnGa/Fe_3Co_5	4.2%	4/4 atoms Co	0.128	0.081	2.54
MnGa/Fe_3Co_5		3/4 atoms Fe	0.135	−0.034	−1.05
MnGa/FeCo		1/1 atom Co	0.131	0.066	2.01
MnGa/FeCo		1/1 atom Fe	0.143	−0.029	−0.87
MnGa/Fe_5Co_3		3/4 atoms Co	0.166	0.075	2.28
MnGa/Fe_5Co_3		4/4 atoms Fe	0.173	−0.037	−1.12
MnGa/Fe		Only Fe	0.159	0.049	1.49

IV. RESULTS AND DISCUSSION

Figure 1 shows the room temperature XRD patterns of $Mn_{1.5}Ga$ thin films as a function of T_s. The two strongest film reflections are indexed to the $L1_0$-$Mn_{1.5}Ga$ crystal structure with a space group of $P4/mmm$ with the (001) reflection at $2\theta = 24.66°$ and the (002) reflection at $2\theta = 50.10°$. Only the MnGa film deposited at $T_s = 450\,°C$ is phase pure. All other films grown at lower or higher substrate temperatures show some traces of Ga and/or Mn. In the following, we report only the physical properties of the sample grown at optimized parameters.

Room-temperature out-of-plane and in-plane hysteresis loops (volume magnetization vs applied magnetic field) for an optimized $Mn_{1.5}Ga$ thin film are shown in Fig. 2(a). The volume magnetization in saturation reaches a maximal value of 840 emu/cm^3, which is very close to the theoretically predicted value. The coercive field in the out-of-plane direction is 6 kOe. The intersection of the out-of-plane (easy axis) and in-plane (hard axis) magnetization curves in saturation occurs at a large anisotropy field (H_s) equal to 5 T, which corresponds to a perpendicular magnetic anisotropy of $K_u \sim 2.10$ MJ/m^3. For details on how to estimate uniaxial magnetic anisotropy from anisotropy field extracted from hysteresis loops, please refer to Ref. [13].

Figure 2(b) shows the angular dependence of the magnetic torque, $T(\varphi)$, for a MnGa thin film while rotating under an applied field of 14 T at 300 K. The data fitting yields a uniaxial magnetic anisotropy of 20.97 Merg/cm^3 (approximately 2.10 MJ/m^3), which is in very good agreement with the estimated value using the anisotropy field extracted from the hysteresis loops. These combined room-temperature magnetic properties with high perpendicular magnetic anisotropy (PMA) and a magnetization close to the theoretical value makes our $L1_0$-$Mn_{1.5}Ga$ films well suited for applications in high-density magnetic recording.

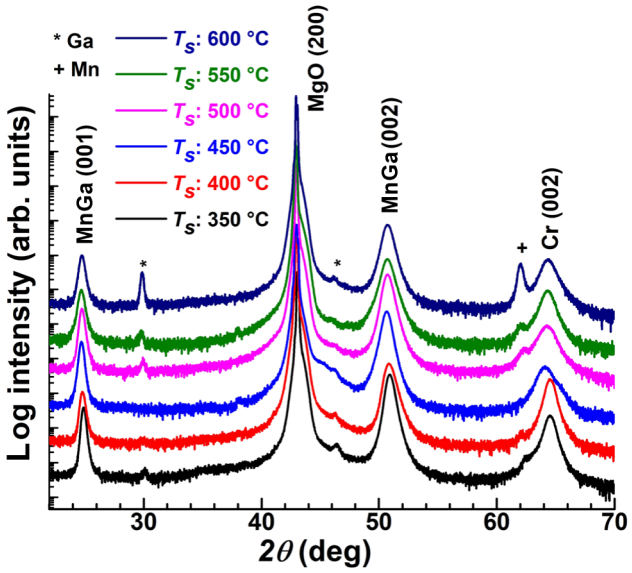

FIG. 1. XRD patterns of epitaxial $Mn_{1.5}Ga$ thin films grown at different T_s from 350 °C to 600 °C.

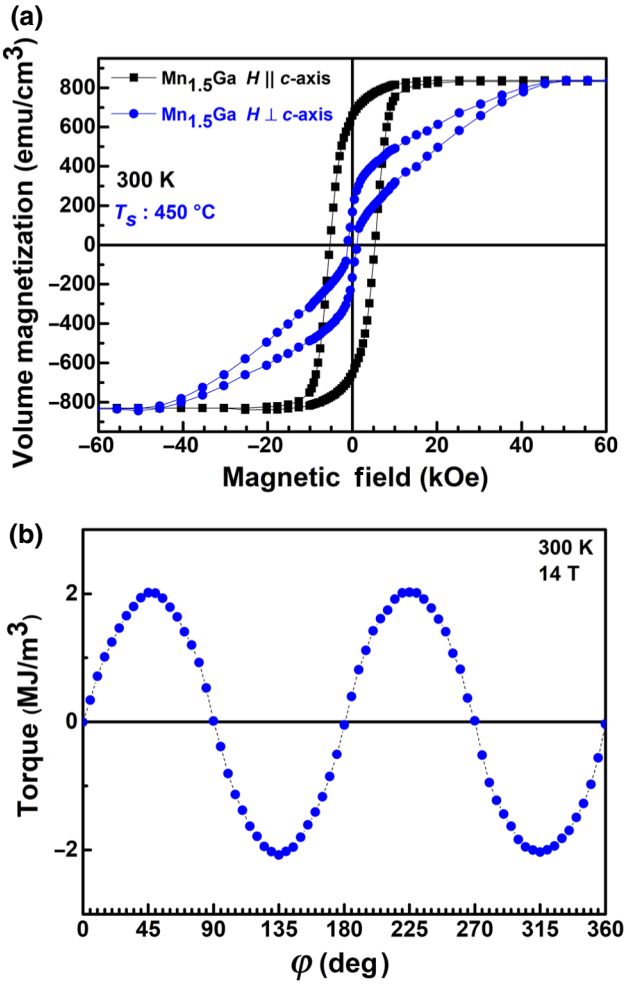

FIG. 2. (a) Out-of-plane and in-plane hysteresis loops for an optimized $Mn_{1.5}Ga$ thin film. (b) Angular dependence of magnetic torque measured for the same sample in a 14-T magnetic field at 300 K.

Figure 3 shows the magnetization data of $Mn_{1.5}Ga$/$Fe_{35}Co_{65}$ epitaxial bilayers with different thicknesses of the FeCo layer. According to the out-of-plane hysteresis loops, the bilayer shows strong exchange coupling with single-phase behavior for a soft magnetic layer thickness of approximately 2 nm, resulting in a nearly 20% increase in volume magnetization from 840 to 1000 emu/cm^3, while the coercivity is preserved at approximately 6 kOe. Further increasing the soft layer thickness deteriorates the coherency of the exchange interaction, as can be seen from the small shoulder in the magnetization data around zero field, which shows that the two layers are not behaving as a single phase under a demagnetizing field. In comparison to our previous exchange spring bilayers in the MnBi/FeCo

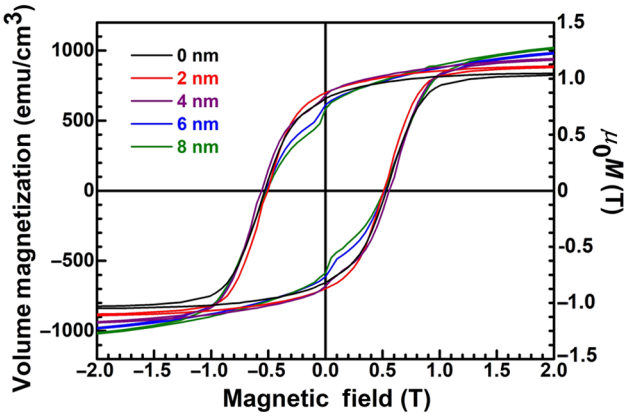

FIG. 3. Out-of-plane magnetization data measured for $Mn_{1.5}Ga/Fe_{35}Co_{65}$ (at. %) epitaxial bilayers with different thicknesses of the soft magnetic layer.

system, the coherency of exchange coupling is improved for the MnGa/FeCo system, allowing a higher critical soft layer thickness. This improvement can be attributed to the epitaxial growth of both hard and soft magnetic layers, leading to a better hard/soft interface quality [39,40].

Cross-sectional HR-TEM images are collected to investigate the hard/soft interface in the bilayer. As shown in Fig. 4(a), the layers are epitaxially grown along the (001) out-of-plane orientation leading to the formation of a smooth interface between MnGa and FeCo layers with a roughness of a few unit cells. The formation of a well-defined interface between MnGa and FeCo layers can also be observed from the high resolution scanning transmission electron microscopy (HR-STEM) image in Fig. 4(b). Moreover, EDX analysis is performed in STEM mode to measure the elemental composition for Cr, Mn, Ga, Fe, and Co in the bilayer sample. The EDX data in Fig. 4(c) show distributions of these elements across the different layers. The measured composition distribution is in good agreement with the different crystalline phases present in each deposited layer. The compositions from EDX analysis correspond to a stoichiometry of $Mn_{1.6}Ga$ and $Fe_{37}Co_{63}$.

The results of our *ab initio* DFT calculations for the MnGa/FeCo interface are summarized in Table I. The values for the interface formation energy, interface exchange coupling energy, and interface exchange constant are calculated for $MnGa/Fe_xCo_{1-x}$ with $x = 0.375$, 0.5, 0.625, and 1.0. Based on the table of cohesive energies [50] as well as our calculations, the surface termination with Ga atoms on the hard magnetic side is always energetically more favorable than a termination with Mn atoms. Nevertheless, we consider both Fe and Co terminations at the interface from the soft magnetic side to compare their effect on the interlayer magnetic exchange coupling. For each atomic termination at the interface, the number of Fe and Co atoms differ.

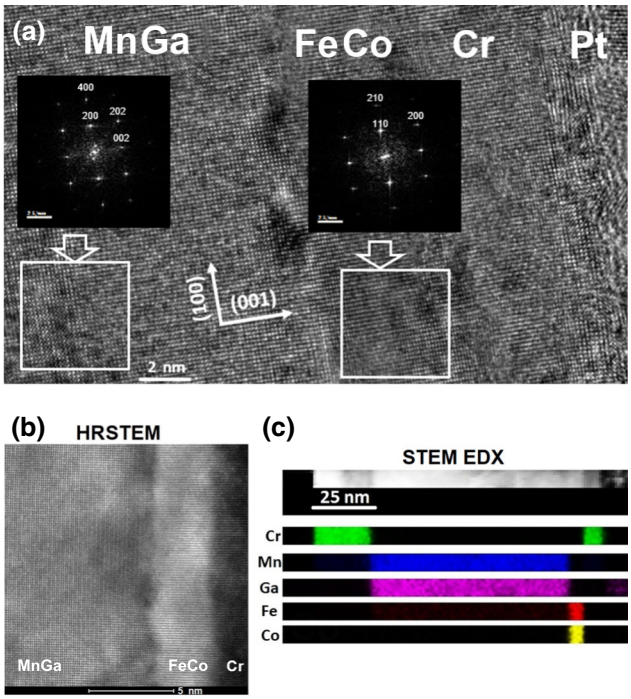

FIG. 4. (a) High-resolution cross-sectional TEM image of $Mn_{1.5}Ga(001)/Fe_{35}Co_{65}(001)$ epitaxial bilayer sample, with 3-nm FeCo thickness; (b) HR-STEM image of the epitaxial MnGa/FeCo interface; and (c) line scan EDS map of the Cr, Mn, Ga, Fe, and Co distribution across the bilayer sample.

In general, the interface made from Co-rich alloys enhances thermodynamic stability since the interfaces with Co termination have lower interface formation energies compared to the ones with Fe termination. Moreover, the calculations show that Co termination at the interface results in significantly improved exchange coupling. On the other hand, the presence of Fe atoms at the interface is in favor of antiferromagnetic coupling. By increasing the number of Fe atoms at the interface, the values of J^{int} and A^{int} both become more negative (except for the pure Fe case, the last row of data in Table I).

In the study by Ma *et al.* [38], it is shown that by increasing the Co content in the FeCo layer above 25%, there is an abrupt transition from FM to AFM for the interface exchange coupling. However, it should be noted that the samples in the study by Ma *et al.* were annealed at 350 °C for 30 min after deposition, while the samples in the current study are not annealed. According to our DFT calculations (Table I), it is evident that the interface exchange coupling is strictly related to the type and concentration of atoms from the soft layer at the interface. Therefore, it is concluded that in the study by Ma *et al.* due to the annealing process, possible diffusion of Fe atoms from the interior layers toward the interface took place, which results in an Fe-rich interface (with a small amount of Co) on the soft magnetic layer side of the exchange interface. This process

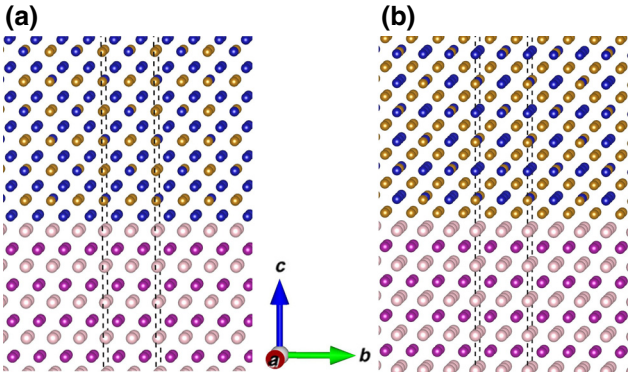

FIG. 5. Atomic structure of (a) MnGa(001)/Fe_3Co_5(001) with Ga and Co terminations, and (b) MnGa(001)/Fe_5Co_3(001) with Ga and Fe terminations demonstrated using Vesta [51]. The Mn, Ga, Fe, and Co atoms are shown with light pink, magenta, yellow, and blue colors, respectively.

leads to a negative interface exchange coupling for samples with more than 25% Co [38] (see Table I, rows 2, 4, and 6). For samples with less than 25% Co, on the other hand, the same thermally induced diffusion results in the presence of only Fe atoms at the vicinity of the interface (Fe termination on the soft layer side). Therefore, based on the last row in Table I for pure Fe, the exchange interaction is completely in favor of ferromagnetic coupling.

Moreover, interface intermixing is also of great importance in the samples that undergo heat treatment. However, this is not the case in the current study. Intermixing again results from the selective interdiffusion of atoms from the interior toward the exchange interface. Depending on the new phase(s) that can form at the interface and the resulting magnetic properties, this newly formed interface region can act either against or in favor of exchange interaction. For instance, Liu *et al.* have shown that in the SmCo/Fe (10-nm) bilayer system, such an intermixed interface improves the exchange coupling since the magnetic properties change gradually at the length scale of 8 nm [42].

Figure 5 shows the atomic structure of MnGa(001)/Fe_3Co_5(001) with Ga and Co terminations as well as MnGa(001)/Fe_5Co_3(001) with Ga and Fe terminations at the interface. Figure 5 indicates that after DFT atomic relaxation, despite 4.2% strain in the *a*-*b* plane at the interfaces, no significant surface reconstruction or irregularity is observed and the experimentally observed epitaxial feature of the interface is preserved with both terminations. It is noted that the results of our DFT calculations, which are obtained at 0 K, are in agreement with the HR-TEM observations (see Fig. 4).

In order to elucidate the effect of soft magnetic layer thickness on the coherency of exchange coupling, scale bridging micromagnetic simulations are performed using the input data of the DFT calculations. As the first

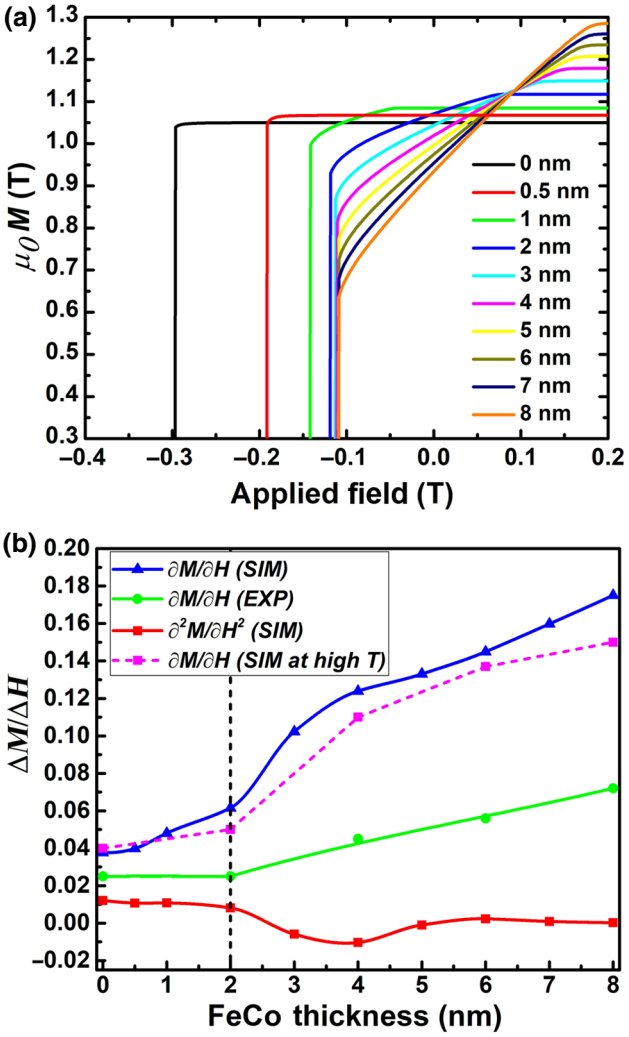

FIG. 6. (a) Simulated hysteresis loops using Oommf code for a MnGa(001)/Fe_3Co_5(001) bilayer system corresponding to the first row of data in Table I for various thicknesses of FeCo layers. (b) First derivative plots of both experimental and simulated hysteresis loops for MnGa(001)/Fe_3Co_5(001) as a function of soft layer thickness. For better visualization, the first derivative at higher temperature and the second derivative of the simulated data are shown as well.

step, using Oommf simulation code, hysteresis graphs for various thicknesses of the Fe_3Co_5 layer are calculated. Figure 6(a) shows the hysteresis loops for a range of FeCo thicknesses from 0 (pure MnGa) to 8 nm. It is found that by increasing the thickness of the FeCo layer, the hysteresis loops no longer show a perfect rectangular shape similar to the pure MnGa layer.

To accurately characterize the effect of increasing soft layer thickness on the degree of exchange coupling, the first and second derivatives of the hysteresis loops in Fig. 6(a) are plotted in Fig. 6(b) as a function of the FeCo layer thickness. For comparison, the first derivative of the experimental hysteresis loops from Fig. 2 is also

included. From the first derivatives, a critical thickness can be defined, below which the hysteresis loop for the exchange coupled bilayer becomes incoherent. The second derivative is shown for a better representation of the incoherency in the case of the simulated hysteresis loops. As it can be observed from Fig. 6(b), at 2-nm thickness of the FeCo layer, the slope of the first derivative rather abruptly increases, which implies a significant decrease in the coherency of exchange coupling. This jump in the plot at 2-nm FeCo thickness can also be observed in the second derivative plot.

Because of the assumption of a perfect single crystalline structure in our micromagnetic simulations at either side of the exchange interface, the simulated graphs generally show lower coercivity values compared to the experimentally measured hysteresis loops. The higher value of coercivity in our experimental samples, which is beneficial as it leads to a higher energy product, is attributed to the possible defects or inhomogeneities present in our samples (e.g., thickness variations, phase segregation, secondary phases, chemical gradients, etc.). Such imperfections result in higher coercivity due to domain-wall pinning. Such inhomogeneities can not only smear the sharpness of the hysteresis curves but can also cause a quasidiscontinuous magnetization (not included in the simulation), which appears as a shoulder around zero field in the experimental data [52]. Since the bilayer samples in the current study are epitaxially grown, as also confirmed by HR-TEM/STEM images, the hard/soft interface is smooth with a roughness of only a few unit cells and, therefore, interface roughness is not considered as a factor affecting the coercivity in MnGa/FeCo bilayers. However, it should be noted that interface roughness is considered the dominant factor deteriorating the exchange coupling in non-epitaxial or polycrystalline bilayers [40].

Based on our micromagnetic simulation data in Fig. 6(a), the coercivity of bilayers decreases as a function of FeCo layer thickness (i.e., increasing volume of the soft magnetic layer), but this effect is only significant for a soft layer thickness below 2 nm (below the exchange length of the hard magnetic MnGa layer, approximately 2.0 nm). Such thickness dependency of coercivity in epitaxial bilayers has been previously reported by Patra *et al.* [53]. This result shows that the simulation model used in our study with the assumption of single crystalline epitaxial bilayers can accurately predict the expected exchange-coupled hysteresis loops for the MnGa/FeCo bilayer system and, therefore, can be reliably used to predict a critical thickness of 2 nm for this system. In comparison, the hysteresis loops collected from our experimental bilayers show nearly no thickness dependency of coercivity (see Fig. 3). The inconsistency suggests that our simplified micromagnetic model can simulate the coercivity values observed in our experimental bilayers with high accuracy in case defects or inhomogeneities are implemented into the simulated structures.

In addition, the simulations are performed at 0 K, while the experimental data are collected at room temperature. Since at higher temperatures both saturation magnetization and anisotropy decrease, we perform the micromagnetic simulations using slightly decreased values (by only 10%) of saturation magnetization (M_s), magnetic anisotropy (k_u), and interface exchange energy (J_{int}) to roughly estimate the effect of slightly higher temperature on the value of critical thickness. As it can be seen in the derivative graphs in Fig. 6(b), at this slightly higher temperature, the resulting derivative graph (magenta dashed line) shows a similar trend as for 0 K only, with slightly smaller derivative values that lie closer to the experimental values (green solid line). Therefore, we conclude that the higher temperature does not affect the critical thickness of 2 nm observed both in experiment and simulation.

The 2-nm critical thickness of the FeCo layer observed for the MnGa/FeCo system is twice the previously reported value of 1 nm in the case of MnBi/FeCo [40]. The improved exchange coupling can be attributed to the similar cubic crystal structure of both MnGa and FeCo with low interfacial strain, which results in the epitaxial growth of FeCo layer. The smooth interface between hard/soft magnetic layers resulting from epitaxial growth improves exchange interactions. Considering the fact that the values of bulk anisotropy and exchange stiffness are rather similar for MnGa and MnBi, our study shows that microstructural factors such as crystalline structure and orientations, interface roughness, and epitaxial growth strongly affect the degree of exchange coupling in multilayer systems. Our 2D model nanostructures can be employed to investigate the controlling structural factors that allow engineering of exchange properties in exchange spring magnets for applications as permanent magnets.

V. CONCLUSION

In summary, we synthesize phase-pure $L1_0$-$Mn_{1.5}Ga$ epitaxial thin films by direct sputtering from a stoichiometric target. The $L1_0$-$Mn_{1.5}Ga$ thin films show a perpendicular coercivity of approximately 6 kOe and a high perpendicular magnetic anisotropy of 2.1 MJ/m^3. Moreover, a high saturation magnetization of 840 emu/cm^3 is measured, which is in very good agreement with the theoretically predicted value. We use these phase-pure highly epitaxial $Mn_{1.5}Ga$ thin films as the hard magnetic phase in a model exchange spring system and couple them to FeCo layers, leading to an approximately 20% increase in overall saturation magnetization and an enhanced total energy product. DFT calculations revealed that a Co-rich soft magnetic layer with Co termination is in favor of coherent interface exchange coupling. Microstructural analysis of the interface using both HR-TEM and micromagnetic simulations show that hard/soft interface properties such as roughness and epitaxial relation are critical to achieve

strong exchange coupling. Experiment and modeling both show that coherent exchange coupling is restricted to a critical thickness of 2 nm for the soft magnetic layer. Our model provides useful guidelines to synthesize exchange-coupled rare-earth-free permanent magnets with a high energy product for applications in renewable energy and spintronics through interface engineering of the hard/soft magnetic layers.

ACKNOWLEDGMENTS

The authors acknowledge the LOEWE project RESPONSE funded by the Ministry of Higher Education, Research and the Arts (HMWK) and the high-performance computer center of Hessen (Lichtenberg).

[1] E. F. Kneller and R. Hawig, The exchange-spring magnet: A new material principle for permanent magnets, IEEE Trans. Magn. **27**, 3588 (1991).

[2] M. J. Kramer, R. W. McCallum, I. A. Anderson, and S. Constantinides, Prospects for non-rare earth permanent magnets for traction motors and generators, JOM **64**, 752 (2012).

[3] D. Li, D. Pan, S. Li, and Z. Zhang, Recent developments of rare-earth-free hard-magnetic materials, Sci. China-Phys. Mech. Astron. **59**, 617501 (2016).

[4] D. Weller, G. Parker, O. Mosendz, E. Champion, B. Stipe, X. Wang, T. Klemmer, G. Ju, and A. Ajan, A HAMR media technology roadmap to an areal density of 4 Tb/in^2, IEEE Trans. Magn. **50**, 3100108 (2014).

[5] H. Pandey, J. Wang, T. Shiroyama, B. S. D. Ch. S. Varaprasad, H. Sepehri-Amin, Y. K. Takahashi, A. Perumal, and K. Hono, Structure optimization of FePt-C nanogranular films for heat assisted magnetic recording media, IEEE Trans. Magn. **52**, 3200108 (2016).

[6] C. Chappert, A. Fert, and F. N. V. Dau, The emergence of spin electronics in data storage, Nat. Mater. **6**, 813 (2007).

[7] S. Mizukami, T. Kubota, F. Wu, X. Zhang, T. Miyazaki, H. Naganuma, M. Oogane, A. Sakuma, and Y. Ando, Composition dependence of magnetic properties in perpendicularly magnetized epitaxial thin films of Mn-Ga alloys, Phys. Rev. B **85**, 014416 (2012).

[8] L. J. Zhu, D. Pan, S. H. Nie, J. Lu, and J. H. Zhao, Tailoring magnetism of multifunctional Mn_xGa films with giant perpendicular anisotropy, Appl. Phys. Lett. **102**, 132403 (2013).

[9] M. Hosoda, M. Oogane, M. Kubota, T. Kubota, H. Saruyama, S. Iihama, H. Naganuma, and Y. Ando, Fabrication of $L1_0$-MnAl perpendicularly magnetized thin films for perpendicular magnetic tunnel junctions, J. Appl. Phys. **111**, 07A324 (2012).

[10] H. Saruyama, M. Oogane, Y. Kurimoto, H. Naganuma, and Y. Ando, Fabrication of $L1_0$-ordered MnAl films for observation of tunnel magnetoresistance effect, Jpn. J. Appl. Phys. **52**, 063003 (2013).

[11] P. Kharel, R. Skomski, R. D. Kirby, and D. J. Sellmyer, Structural, magnetic and magneto-transport properties of Pt-alloyed MnBi thin films, J. Appl. Phys. **107**, 09E303 (2010).

[12] W. Zhang, P. Kharel, S. Valloppilly, L. Yue, and D. J. Sellmyer, High-energy-product MnBi films with controllable anisotropy, Phys. Status Solidi B **252**, 1934 (2015).

[13] S. Sabet, E. Hildebrandt, F. M. Romer, I. Radulov, H. Zhang, M. Farle, and L. Alff, Low-temperature phase *c*-axis oriented manganese bismuth thin films with high anisotropy grown from an alloy $Mn_{55}Bi_{45}$ target, IEEE Trans. Magn. **53**, 2100306 (2017).

[14] X. S. Lu, J. K. Liang, and M. G. Zhou, *ASM Metals Hand Book: Volume 3 - Alloy Phase Diagrams* (ASM Internationals, Materials Park, Russell Township, Geauga County, Ohio, USA, 1980).

[15] H. G. Meissner, K. Schubert, and T. R. Anantharaman, The constitution and structure of manganese-gallium alloys, Proc. Indian Acad. Sci. **61**, 340 (1965).

[16] T. B. Massalski, *Binary Alloy Phase Diagrams* (Materials Information Society, Ohio, 1990). 2nd ed.

[17] S. Mizukami, F. Wu, A. Sakuma, J. Walowski, D. Watanabe, T. Kubota, X. Zhang, H. Naganuma, M. Oogane, Y. Ando, and T. Miyazaki, Long-Lived Ultrafast Spin Precession in Manganese Alloys Films with a Large Perpendicular Magnetic Anisotropy, Phys. Rev. Lett. **106**, 117201 (2011).

[18] A. Sakuma, Electronic structures and magnetism of CuAu-type MnNi and MnGa, J. Magn. Magn. Mater. **187**, 105 (1998).

[19] L. J. Zhu, S. H. Nie, K. K. Meng, D. Pan, J. H. Zhao, and H. Z. Zheng, Multifunctional $L1_0$-$Mn_{1.5}Ga$ films with ultrahigh coercivity, giant perpendicular magnetocrystalline anisotropy and large magnetic energy product, Adv. Mater. **24**, 4547 (2012).

[20] Z. Yang, J. Li, D. Wang, K. Zhang, and X. Xie, Electronic structure and magnetic properties of δ-MnGa, J. Magn. Magn. Mater. **182**, 369 (1998).

[21] L. J. Zhu and J. H. Zhao, Perpendicularly magnetized Mn_xGa films: Promising materials for future spintronic devices, magnetic recording and permanent magnets, Appl. Phys. A **111**, 379 (2013).

[22] J. Winterlik, B. Balke, G. H. Fecher, C. Felser, M. C. M. Alves, F. Bernardi, and J. Morais, Structural, electronic, and magnetic properties of tetragonal $Mn_{3-x}Ga$: Experiments and first-principles calculations, Phys. Rev. B **77**, 054406 (2008).

[23] K. M. Krishnan, Ferromagnetic $\delta Mn_{1-x}Ga_x$ thin films with perpendicular anisotropy, Appl. Phys. Lett. **61**, 2365 (1992).

[24] M. Tanaka, J. P. Harbison, J. DeBoeck, T. Sands, B. Philips, T. L. Cheeks, and V. G. Keramidas, Epitaxial MnGa/NiGa magnetic multilayers on GaAs, Appl. Phys. Lett. **62**, 696 (1993).

[25] E. Lu, D. C. Ingram, A. R. Smith, J. W. Knepper, and F. Y. Yang, Reconstruction Control of Magnetic Properties during Epitaxial Growth of Ferromagnetic $Mn_{3-\delta}Ga$ on Wurtzite GaN(0001), Phys. Rev. Lett. **97**, 146101 (2006).

[26] A. Bedoya-Pinto, C. Zube, J. Malindretos, A. Urban, and A. Rizzi, Epitaxial $\delta - Mn_xGa_{1-x}$ layers on GaN(0001): Structural, magnetic, and electrical transport properties, Phys. Rev. B **84**, 104424 (2011).

[27] A. W. Arins, H. F. Jurca, J. Zarpellon, J. Varalda, I. L. Graff, W. H. Schreiner, and D. H. Mosca, Structure and magnetism of MnGa ultra-thin films on GaAs(111)B, IEEE Trans. Magn. **49**, 5595 (2013).

[28] K. Wang, E. Lu, J. W. Knepper, F. Yang, and A. R. Smith, Structural controlled magnetic anisotropy in Heusler $L1_0$-MnGa epitaxial thin films, Appl. Phys. Lett. **98**, 162507 (2011).

[29] E. Feng, D. V. Thiet, D. D. Dung, Y. Shin, and S. Chob, Substrate-modified ferrimagnetism in MnGa films, J. Appl. Phys. **108**, 113903 (2010).

[30] K. Wang, A. Chinchore, W. Lin, D. C. Ingram, A. R. Smith, A. J. Hauser, and F. Yang, Epitaxial growth of ferromagnetic δ-phase manganese gallium on semiconducting scandium nitride(001), J. Cryst. Growth **311**, 2265 (2009).

[31] M. Glas, I.-M. Imort, P. Thomas, G. Reiss, and D. Ebke, Anomalous hall effect in perpendicularly magnetized $Mn_{3-x}Ga$ thin films, J. Magn. Magn. Mater. **333**, 134 (2013).

[32] E. E. Fullerton, J. S. Jiang, M. Grimsditch, C. H. Sowers, and S. D. Bader, Exchange-spring behaviour in epitaxial hard/soft magnetic bilayers, Phys. Rev. B **58**, 12193 (1998).

[33] E. E Fullerton, J. S Jiang, and S. D Bader, Hard/soft magnetic heterostructures: Model exchange-spring magnets, J. Magn. Magn. Mater. **200**, 392 (1999).

[34] T. Leineweber and H. Kronmüller, Micromagnetic examination of exchange coupled ferromagnetic nanolayers, J. Magn. Magn. Mater. **176**, 145 (1997).

[35] R. Skomski and J. M. D. Coey, Giant energy product in nanostructured two-phase magnets, Phys. Rev. B **48**, 15812 (1993).

[36] R. Skomski, Aligned two-phase magnets: Permanent magnetism of the future? (invited), J. Appl. Phys. **76**, 7059 (1994).

[37] L. H Lewis and Félix Jiménez-Villacorta, Perspectives on permanent magnetic materials for energy conversion and power generation, Metall. Mater. Trans. A **44**, 2 (2013).

[38] Q. L. Ma, S. Mizukami, T. Kubota, X. M. Zhang, Y. Ando, and T. Miyazaki, Abrupt Transition from Ferromagnetic to Antiferromagnetic of Interfacial Exchange in Perpendicularly Magnetized $L1_0$-MnGa/FeCo Tuned by Fermi Level Position, Phys. Rev. Lett. **112**, 157202 (2014).

[39] S. Sabet, E. Hildebrandt, and L. Alff, Synthesis and magnetic properties of the thin film exchange spring system of MnBi/FeCo, J. Phys. Conf. **903**, 012032 (2017).

[40] S. Sabet, A. Moradabadi, S. Gorji, M. Yi, Q. Gong, M. H. Fawey, E. Hildebrandt, D. Wang, H. Zhang, B.-X. Xu, C. Kübel, and L. Alff, Impact of interface structure on magnetic exchange coupling in MnBi/Fe_xCo_{1-x} bilayers, Phys. Rev. B **98**, 174440 (2018).

[41] J. S. Jiang, J. E. Pearson, Z. Y. Liu, B. Kabius, S. Trasobares, D. J. Miller, S. D. Bader, D. R. Lee, D. Haskel, G. Srajer, and J. P. Liu, Improving exchange-spring nanocomposite permanent magnets, Appl. Phys. Lett. **85**, 5293 (2004).

[42] Yaohua Liu, S. G. E. Te Velthuis, J. S. Jiang, Y. Choi, S. D. Bader, A. A. Parizzi, H. Ambaye, and V. Lauter, Magnetic structure in Fe/Sm-Co exchange spring bilayers with intermixed interfaces, Phys. Rev. B **83**, 174418 (2011).

[43] G. Kresse and J. Furthmüller, Efficient iterative schemes for *ab initio* total-energy calculations using a plane-wave basis set, Phys. Rev. B **54**, 11169 (1996).

[44] J. P. Perdew, K. Burke, and M. Ernzerhof, Generalized Gradient Approximation Made Simple, Phys. Rev. Lett. **77**, 3865 (1996).

[45] M. J. Donahue and D. G. Porter, OOMMF Software Package, 2016.

[46] T. H. Rana, P. Manchanda, B. Balamurugan, A. Kashyap, T. R. Gao, I. Takeuchi, J. Cun, S. Biswas, R. F. Sabirianov, D. J. Sellmyer, and R. Skomski, Micromagnetism of MnBi:Fe-Co thin films, J. Phys. D: Appl. Phys. **49**, 075003 (2016).

[47] S. Mao, J. Lu, X. Zhao, X. Wang, D. Wei, J. Liu, Ji Xia, and J. Zhao, MnGa-based fully perpendicular magnetic tunnel junctions with ultrathin Co_2MnSi interlayers, Sci. Rep. **7**, 43064 (2017).

[48] N. Umetsu, A. Sakuma, and Y. Toga, First-principles study of interface magnetic structure in $Nd_2Fe_{14}B$/(Fe,Co) exchange spring magnets, Phys. Rev. B **93**, 014408 (2016).

[49] Y. Toga, H. Moriya, H. Tsuchiura, and A. Sakuma, First principles study on interfacial electronic structures in exchange-spring magnets, J. Phys. Conf. Ser. **266**, 012046 (2011).

[50] C. Kittel, *Introduction to Solid State Physics* (Wiley, Hoboken, New Jersey, USA, 1953).

[51] K. Momma and F. Izumi, VESTA 3 for three-dimensional visualization of crystal, volumetric and morphology data, J. Appl. Crystallogr. **44**, 1272 (2011).

[52] R. Skomski, Nanomagnetics, J. Phys. Condens. Matter **15**, R841 (2003).

[53] A. K. Patra, F. Fleischhauer, S. Oswald, L. Schultz, and V. Neu, Coercivity mechanism in hard magnetic $SmCo_5$/$PrCo_5$ bilayers, J. Phys. D: Appl. Phys. **47**, 215001 (2014).